AGU PUBLICATIONS

JGR

Journal of Geophysical Research: Space Physics

RESEARCH ARTICLE
10.1002/2015JA021213

Key Points:
- Dipolarization fronts as earthward propagating flux ropes
- Three-dimensional global hybrid simulation of dipolarization fronts
- Formation, structure, and evolution of dipolarization fronts

Supporting Information:
- Figure S1
- Text S1

Correspondence to:
Q. Lu,
qmlu@ustc.edu.cn

Citation:
Lu, S., et al. (2015), Dipolarization fronts as earthward propagating flux ropes: A three-dimensional global hybrid simulation, *J. Geophys. Res. Space Physics*, *120*, 6286–6300, doi:10.1002/2015JA021213.

Received 16 MAR 2015
Accepted 18 JUL 2015
Accepted article online 22 JUL 2015
Published online 17 AUG 2015

Dipolarization fronts as earthward propagating flux ropes: A three-dimensional global hybrid simulation

San Lu[1,2], Quanming Lu[1,2], Yu Lin[3], Xueyi Wang[3], Yasong Ge[4], Rongsheng Wang[4], Meng Zhou[5], Huishan Fu[6], Can Huang[1], Mingyu Wu[1], and Shui Wang[1]

[1]CAS Key Laboratory of Geospace Environment, Department of Geophysics and Planetary Sciences, University of Science and Technology of China, Hefei, China, [2]Collaborative Innovation Center of Astronautical Science and Technology, Harbin, China, [3]Physics Department, Auburn University, Auburn, Alabama, USA, [4]Key Laboratory of Earth and Planetary Physics, Institute of Geology and Geophysics, Chinese Academy of Sciences, Beijing, China, [5]Institute of Space Science and Technology, Nanchang University, Nanchang, China, [6]Space Science Institute, School of Astronautics, Beihang University, Beijing, China

Abstract Dipolarization fronts (DFs) as earthward propagating flux ropes (FRs) in the Earth's magnetotail are presented and investigated with a three-dimensional (3-D) global hybrid simulation for the first time. In the simulation, several small-scale earthward propagating FRs are found to be formed by multiple X line reconnection in the near tail. During their earthward propagation, the magnetic field B_z of the FRs becomes highly asymmetric due to the imbalance of the reconnection rates between the multiple X lines. At the later stage, when the FRs approach the near-Earth dipole-like region, the antireconnection between the southward/negative B_z of the FRs and the northward geomagnetic field leads to the erosion of the southward magnetic flux of the FRs, which further aggravates the B_z asymmetry. Eventually, the FRs merge into the near-Earth region through the antireconnection. These earthward propagating FRs can fully reproduce the observational features of the DFs, e.g., a sharp enhancement of B_z preceded by a smaller amplitude B_z dip, an earthward flow enhancement, the presence of the electric field components in the normal and dawn-dusk directions, and ion energization. Our results show that the earthward propagating FRs can be used to explain the DFs observed in the magnetotail. The thickness of the DFs is on the order of several ion inertial lengths, and the electric field normal to the front is found to be dominated by the Hall physics. During the earthward propagation from the near-tail to the near-Earth region, the speed of the FR/DFs increases from ~150 km/s to ~1000 km/s. The FR/DFs can be tilted in the GSM (x, y) plane with respect to the y (dawn-dusk) axis and only extend several Earth radii in this direction. Moreover, the structure and evolution of the FRs/DFs are nonuniform in the dawn-dusk direction, which indicates that the DFs are essentially 3-D.

1. Introduction

Flux ropes (FRs) are three-dimensional (3-D) helical magnetic structures generated by magnetic reconnection with multiple X lines [e.g., *Schindler*, 1974; *Lee and Fu*, 1985; *Zhu and Winglee*, 1996; *Daughton et al.*, 2011]. In spacecraft observations of the Earth's magnetotail, FRs are mainly characterized by a well-defined bipolar B_z signature and widely believed to play a critical role in the energy transport during substorms [e.g., *Baker et al.*, 1996] and the generation of energetic particles [e.g., *Wang et al.*, 2010a, 2010b]. In early times when the concept of FRs/plasmoids was first put forward for the magnetotail, they were believed to be driven only tailward by the pressure gradient and magnetic tension forces [*Hones*, 1977; *Moldwin and Hughes*, 1991]. However, later on, observations of both tailward and earthward propagating FRs in the magnetotail were reported by *Moldwin and Hughes* [1994]. Based on Geotail observations, *Slavin et al.* [2003] further studied the FRs in the magnetotail and divided them into two categories: tailward propagating (plasmoid-type) and earthward propagating (bursty bulk flow (BBF)-type) FRs. The earthward propagating FRs are also observed by other spacecraft, e.g., Cluster [*Zong et al.*, 2004; *Eastwood et al.*, 2005] and Time History of Events and Macroscale Interactions during Substorms (THEMIS) [*Imber et al.*, 2011].

Dipolarization fronts (DFs), on the other hand, are also frequently observed in the Earth's magnetotail plasma sheet [*Nakamura et al.*, 2002; *Ohtani et al.*, 2004; *Runov et al.*, 2009; *Schmid et al.*, 2011] during BBF events [*Angelopoulos et al.*, 1994]. DFs play important roles in the transport of magnetic flux and energy [*Volwerk et al.*, 2008; *Nakamura et al.*, 2011; *Hamrin et al.*, 2013] and the particle acceleration

[*Deng et al*., 2010; *Zhou et al*., 2010; *Ashour-Abdalla et al*., 2011; *Fu et al*., 2011; *Artemyev et al*., 2012; *Wu et al*., 2013; *Birn et al*., 2014] during substorms. They are mostly observed near the leading edge of earthward high-speed flows (or BBFs), and characterized by a sharp enhancement of B_z, which is usually preceded by a smaller amplitude B_z dip. The earthward propagation of the DFs is also reported based on THEMIS observations [*Runov et al*., 2009, 2011a, 2011b]. It is readily noted that DFs share many similarities with the earthward propagating FRs in their observational signatures, such as the well-defined negative-then-positive B_z signatures and the coexisted high-speed earthward plasma flows, which imply that there might be a deeper connection between the earthward propagating FRs and DFs. Recently, based on THEMIS observations, *Vogiatzis et al*. [2011, 2015] suggest that there is a possibility that DFs are originated from highly dissipated FRs during the late stage of their evolution. Previously, by performing a 3-D global hybrid simulation [*Lin et al*., 2014], we have investigated the DF in the near-Earth region at $x \approx -10R_E$ near the global dipolarization front [*Baumjohann et al*., 1999], where oscillation of the DF is found to be developed by the fast-flow braking, with a significant short-scale length dip of B_z. More recently, the evolution of the FRs in the magnetotail has also been studied with the 3-D global hybrid simulation [*Lu et al*., 2015].

In this paper, we investigate the connection between the FRs and DFs in the magnetotail plasma sheet with the 3-D global hybrid simulation. It is found that several small-scale earthward propagating FRs are formed by multiple X line reconnection in the near tail at $x \approx -20R_E$, and these FRs gradually evolve into DFs with highly asymmetric north-south magnetic field B_z during their earthward propagation. The simulation shows that the earthward propagating FRs can fully reproduce the observational features of DFs and thus can be used to explain the DFs observed in the magnetotail. Moreover, the kinetic structure, global-scale evolution, and merging of DFs (or earthward propagating FRs) at $x \approx -10R_E$ are investigated in present study. The outline of this paper is as follows: the global hybrid model is described in section 2. The simulation results are presented in section 3. Section 4 contains the discussion, and a summary is given in section 5.

2. Simulation Model

The simulation model used in this study is a 3-D global hybrid simulation model which contains the whole magnetosphere and has been described in detail in our earlier studies [*Lin et al*., 2014; *Lu et al*., 2015]. The simulation domain is a cuboid box in the GSM coordinate system, with $-60R_E \le x \le 20R_E$ and $-30R_E \le y$, $z \le 30R_E$. Nonuniform Cartesian cell grids are used, with a resolution of $\Delta x = \Delta y = \Delta z = 0.15R_E$ in the near tail. A lower resolution is adopted in the lobes and higher resolution $0.09R_E$ around the dayside magnetopause. The cell dimensions are $n_x \times n_y \times n_z = 373 \times 217 \times 217$. A total of 3×10^9 particles are employed. The typical time step is $\Delta t = 0.05\Omega_0^{-1}$. In addition to the ion particles, a cold, incompressible ion fluid dominates the inner magnetosphere with $r < 6R_E$.

Initially, a dipole geomagnetic field is implemented at $x < 15R_E$, along with an image dipole. A uniform solar wind with convection speed $V_0 = 700$ km/s, ion number density $N_0 = 6$ cm^{-3}, temperature $T_{i0} = 10$ eV, and the interplanetary magnetic field (IMF) $\mathbf{B}_0 = (0, 0, -10$ nT) are specified at $x > 15R_E$. The corresponding solar wind ion gyrofrequency $\Omega_0 = 0.958$ s^{-1}, and Alfvén speed $V_{A0} = 89$ km/s. A small current-dependent collision frequency, $\nu \approx 0.01\Omega j/j_0$, is imposed to simulate the anomalous resistivity and trigger magnetic reconnection in the simulation (here Ω is the local ion gyrofrequency, $j_0 = B_0/\mu_0 d_{i0}$, and $d_{i0} = c/\Omega_{pi0}$ is the ion inertial length of the solar wind). The solar wind flows along the $-x$ direction from the dayside boundary at $x = 20R_E$, carrying the steady IMF. Open boundary conditions are used for the rest five boundaries. At the inner boundary $r = 3.5R_E$, particles are reflected, and a magnetospheric-ionospheric electrostatic coupling model is employed. In the present study, a uniform ionospheric Pederson conductance $\Sigma_P = 5$ S is adopted, and the Hall conductance Σ_H is assumed to be zero.

In 3-D global hybrid simulations, because of the huge amount of computation and data storage, it is unfeasible to use a realistic solar wind ion inertial length in the 3-D global hybrid simulation. Therefore, in our simulation, the solar wind ion inertial length is chosen as $d_{i0} = 0.1R_E$. As illustrated in our previous paper [*Lin et al*., 2014], the magnetosphere in our simulation is Earth-like based on the scaling study of *Omidi et al*. [2006], although this d_{i0} is 6.77 times larger than the realistic value. As the solar wind ion inertial length is $d_{i0} = 0.1$ R_E, and the peak ion number density in the plasma sheet is on the order of $0.1N_0$ (N_0 is the solar wind ion number density), so the ion inertial length in the magnetotail is $0.25R_E \sim 0.55R_E$

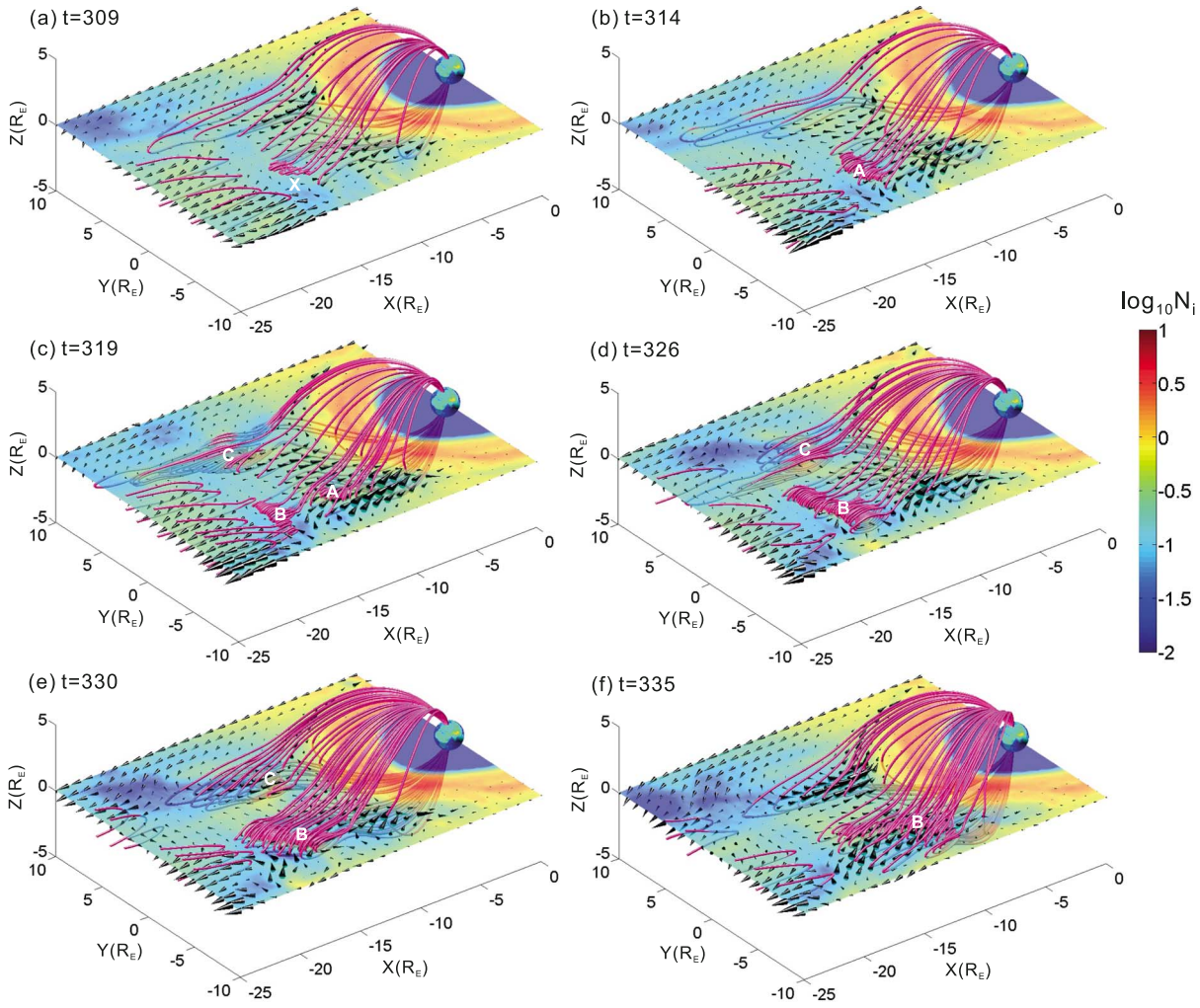

Figure 1. Magnetic field lines, ion flow vectors in 3-D perspective, and ion density $\log_{10}N_i$ contours in zoomed near-tail region of the equatorial plane at (a) t =309, (b) 314, (c) 319, (d) 326, (e) 330, and (f) 335. The label "*X*" denotes the location of the reconnection X line, and A, B, and C denote the earthward propagating FRs.

[*Lin et al.*, 2014]. Therefore, our grid size $\Delta x = \Delta y = \Delta z = 0.15R_E$ is small enough to resolve the ion kinetic physics in the magnetotail. Based on the computer resource at the moment, we also perform three more runs with larger grid sizes, $0.2R_E$, $0.4R_E$, and $0.8R_E$. A convergent study of the four runs with different grid sizes is included in the supporting information of this article online. Physical quantities are normalized as follows. The magnetic field B is normalized to the IMF B_0, the ion number density to the solar wind density N_0, and the time t to Ω_0^{-1}. The spatial coordinates are expressed in units of R_E, the velocities are in units of V_{A0}, and the electric field is in units of $V_{A0}B_0$.

3. Simulation Results

In the simulation, the magnetosphere is formed self-consistently by the interaction between the solar wind and the geomagnetic field. At about t =200, well-developed bow shock, magnetosheath, and magnetosphere configurations are obtained, and a long stretched current sheet is formed in the magnetotail. During the continuous thinning of the current sheet, magnetic reconnection occurs in the near tail. Figure 1 shows 3-D magnetic field lines, ion flow vectors, and ion density $\log_{10}N_i$ contours in the zoomed near-tail region of equatorial plane (z = 0) at t =309 (Figure 1a), 314 (Figure 1b), 319 (Figure 1c), 326 (Figure 1d), 330 (Figure 1e), and 335 (Figure 1f). At t =309, a tiny seed FR is formed in the vicinity of the X line around $x = -16.5\ R_E$. The FR (denoted by "A") gains more magnetic flux and grows larger with the proceeding of the multiple X line

reconnection. At t=314, FR-A is well developed and flanked by two X lines, the primary X line (with a faster reconnection rate) at $x \approx -18R_E$ and the secondary X line (with a slower reconnection rate) at $x \approx -14R_E$. At t=319, FR-A moves to $x \approx -14R_E$, and the primary reconnection diffusion region is elongated during this process. With the earthward propagation of FR-A, reconnection at the secondary X line is gradually suppressed and evolves into antireconnection (for "antireconnection," see, e.g., *Oka et al.* [2010]) due to the driven of the earthward high-speed flow of the primary X line. Here antireconnection refers to the reconnection between the southward/negative B_z of the FR and the northward/positive geomagnetic field, which distinguish from the conventional magnetotail reconnection between the $\pm B_x$ magnetic field lines. In the elongated diffusion region, a new FR denoted by "B" is formed at $x \approx -18R_E$. Note that there is another FR denoted by "C" located on the duskside section at $x \approx -15R_E$, $y \approx 5R_E$. At t=326, FR-B grows larger and gradually moves to $x \approx -17R_E$, while FR-A has already merged into the near-Earth region through the antireconnection. At t=330, FR-B and FR-C become highly asymmetric, with northward magnetic flux much larger than southward magnetic flux, as some of the southward magnetic flux has been eroded by the antireconnection process. As the proceeding of the antireconnection, at t=335, FR-C has fully merged into the near-Earth region, while the leading edge of FR-B also begins to merge.

Note that the ion density in the magnetotail plasma sheet is typically 0.1 N_0; the local ion inertial length is thus $d_i \approx 0.3d_{i0} = 0.3R_E$. In the ambient and lobe regions, the ion inertial length is even higher because of the lower density. Furthermore, in the plasma sheet, near the magnetic field reversal, the particles move in meandering orbits instead of the Larmor motion. And the ion meandering (bouncing) half width of the B_x reversal is [*Kuznetsova et al.*, 2001]

$$\lambda_{iz} = \left(\frac{2m_iT_i}{e^2(\partial B_x/\partial z)^2}\right)^{1/4} \approx \left(\frac{2m_iT_i}{e^2B_x^2/\delta^2}\right)^{1/4}.$$

Given the ion temperature in the plasma sheet $T_i \approx 2$ keV, the ambient magnetic field $B_x \approx 35$ nT, and the half width of the plasma sheet δ is about $0.5R_E$, one can calculate $\lambda_{iz} \approx 0.8R_E$. On the other hand, in the ambient region of the plasma sheet where the magnetic field is stronger, the motion of the ions is the Larmor motion, and the Larmor radius is calculated $\rho_i \approx 0.2R_E$. Our grid size in the near-tail plasma sheet $\Delta x = \Delta y = \Delta z = 0.15R_E$, smaller than the inertial length and the Larmor radius of ions, is thus sufficiently small to resolve the ion kinetic physics in the magnetotail plasma sheet.

Figure 2 shows the evolution of B_z and ion flow vectors in the near tail of the equatorial plane at t=308, 312, 316, 320, 324, 328, 332, 335, and 338. In the figure, the FRs are characterized by the bipolar B_z structures. At t=308, according to the coincident reversals of B_z and V_{ix}, a near-tail reconnection is in progress at $x \approx -17R_E$, with the X line stretching from about $y = -10R_E$ to $2R_E$. At t=312, FR-A is formed in the vicinity of the X line at $x \approx -16.5R_E$, and the spatial scale of the FR in the y direction is several Earth radii. The FR is embedded in the earthward high-speed flow (or BBF) and propagates earthward. By t=316, FR-A has moved to $x \approx -15R_E$ and begins to show a stronger asymmetry of B_z. At t=320, FR-A has continued to move to $x \approx -13R_E$ and becomes even more asymmetric. At the same time, FR-B are newly formed at $x \approx -18R_E$, which extends from $y = -9R_E$ to $-2R_E$ in the dawn-dusk direction. From t=320 to 324, FR-A gradually merges into the near-Earth region, while FR-B grows stronger and moves earthward slowly. From t=328, FR-B begins to move faster toward the near-Earth region and eventually merges into this region at about t=338. FR-C is formed at about t=308 and stays at $x \simeq -15R_E$ as a quasi-static structure until t=324. At t=328, the earthward flow becomes stronger which drives FR-C earthward quickly. FR-C becomes highly asymmetric and eventually merges into the near-Earth region at about t=335. Obviously, the above earthward propagating FRs, at the later stage of their evolution, share many similarities with the observed DFs [e.g., *Runov et al.*, 2009; *Schmid et al.*, 2011; *Fu et al.*, 2012b], such as a sharp enhancement of B_z, a smaller amplitude B_z dip, and the corresponding high-speed earthward flow. We suggest that the DFs are actually earthward propagating FRs in the magnetotail, and hereinafter we do not distinguish them in this paper.

In order to further demonstrate that the above earthward propagating FRs are DFs, we assume three virtual satellites located at P1 $((-16, -5, 0)R_E)$, P2 $((-18, -5, 0)R_E)$, and P3 $((-12, 2, 0)R_E)$, which are marked in Figure 2 by symbols of diamond, asterisk, and triangle, respectively. Figure 3 shows the magnetic field components B_x, B_y, and B_z; ion flow velocities V_{ix}, V_{iy}, and V_{iz}; and electric field components E_x and E_y

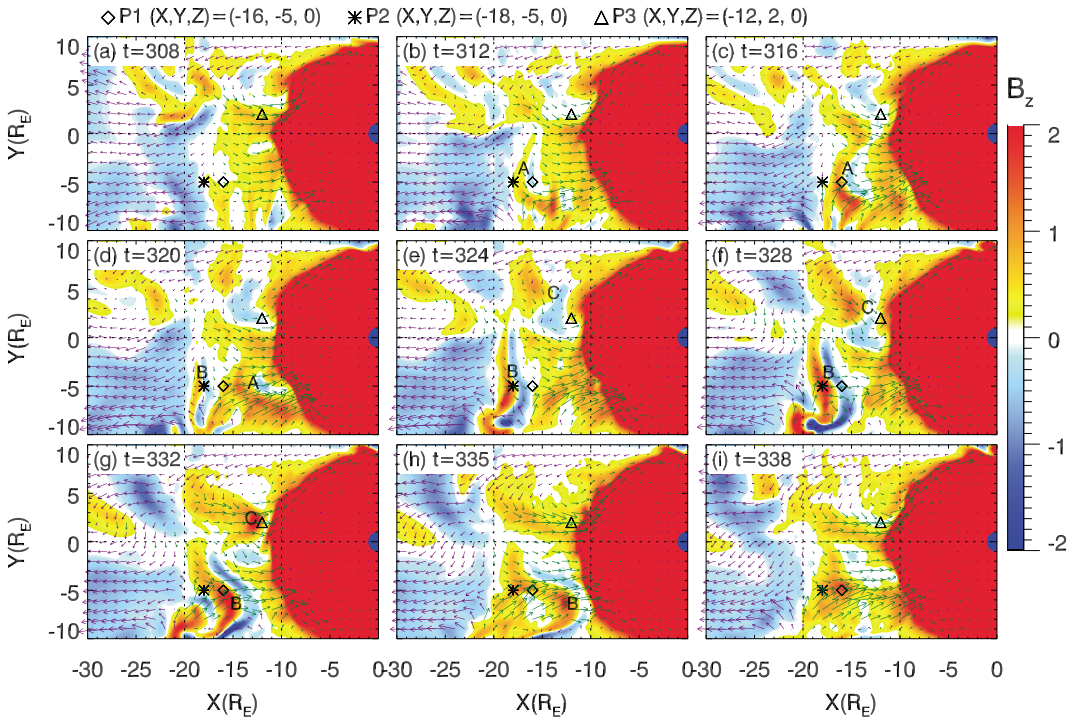

Figure 2. Contour of the B_z component and projection of the ion flow vectors in the near-tail region of the equatorial plane at (a) t =308, (b) 312, (c) 316, (d) 320, (e) 324, (f) 328, (g) 332, (h) 335, and (i) 338. The labels A, B, and C denote the three DFs (or earthward propagating FRs). The green and violet arrows show the flow vectors that are pointing earthward and tailward, respectively.

versus time at the three locations. At P1 ($(-16, -5, 0)R_E$), the two DFs, DF-A and DF-B, are successively observed at about t =315 and 330, respectively. The features of the sharp enhancement of B_z and the preceding smaller-amplitude negative B_z dip are both reproduced. From the virtual observation of the ion flow velocity, the earthward fast flows (BBF-A and BBF-B) arise slightly ahead of the arrival of the DFs (DF-A and DF-B), which is consistent with THEMIS observations [*Runov et al.*, 2009] and magnetohydrodynamic (MHD) simulations [*Ge et al.*, 2011]. Note that the magnetic field is normalized to

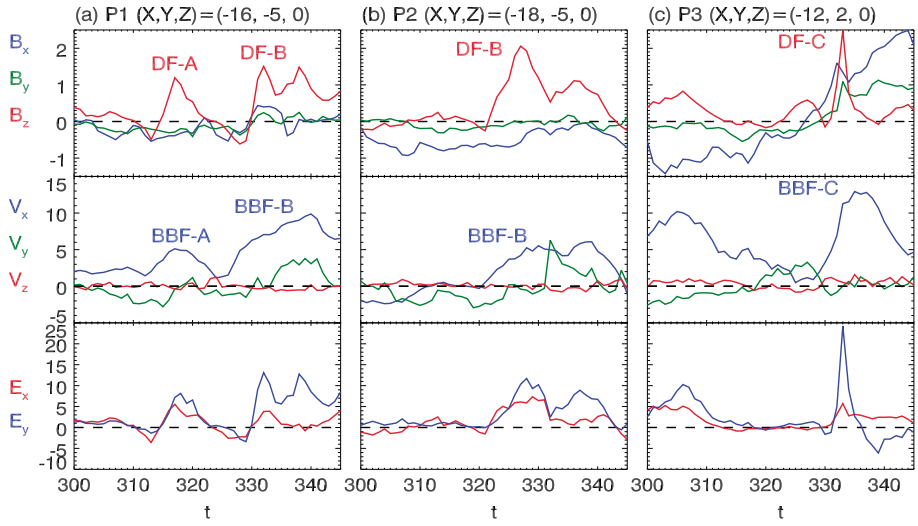

Figure 3. Virtual satellite observations of the magnetic field components B_x, B_y, and B_z; ion flow velocities V_{ix}, V_{iy}, and V_{iz}; and electric field components E_x and E_y versus time at three locations: (a) P1 ($(-16, -5, 0)R_E$), (b) P2 ($(-18, -5, 0)R_E$), and (c) P3 ($(-12, 2, 0)R_E$), which are marked in Figure 2 by symbols of diamond, asterisk, and triangle, respectively.

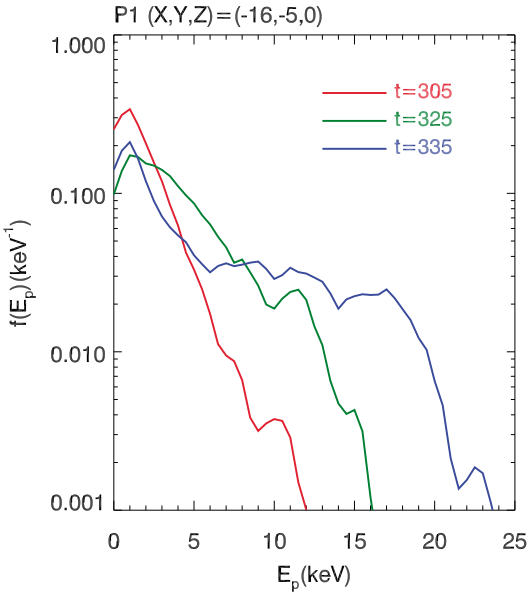

Figure 4. Normalized ion energy spectra at P1 ($(-16,-5,0)R_E$), at t=305 (in front of DF-A), 325 (between DF-A and DF-B), and 335 (behind DF-B).

the IMF B_0 (=10 nT) and the velocity is normalized to the solar wind Alfvén speed V_{A0} (=89 km/s). Therefore, the B_z peaks of DF-A and DF-B are about 13 nT and 15 nT, and the corresponding BBF-A and BBF-B have the V_{ix} peaks of about 450 km/s and 900 km/s. The electric field components E_x and E_y increase on the DFs. Because DF-A is formed at about $x=-16.5R_E$ and propagates earthward, only DF-B (formed at about $x=-18R_E$) can be observed at P2 ($(-18,-5,0)R_E$). At P3 ($(-12,2,0)R_E$), a sharper and stronger DF (DF-C) accompanied by a strong BBF (BBF-C) is observed. The B_z peak of DF-C is about 25 nT, and the V_{ix} peak of BBF-C is about 1150 km/s. Figure 4 depicts the normalized ion energy spectra at P1 ($(-16,-5,0)R_E$), at t=305 (in front of DF-A), 325 (between DF-A and DF-B), and 335 (behind DF-B). It shows that after the passage of DF-A, the ions around P1 are more energetic. At t=335, after the passage of DF-B, the ions around P1 are further energized. The ion energy jumps after the passages of DF-A and DF-B are consistent with the point that the DF is a boundary layer separating the lower-energy ambient plasma sheet from the higher-energy BBF plasma [e.g., *Runov et al.*, 2011a].

The structures of magnetic field B_z, electric field E_x, ion flow velocity V_{ix}, and the magnetic field lines around FR/DF-B in the (x,z) plane along $y=-5R_E$ at t=330 are presented in detail in Figure 5. According to the reversal of V_{ix} (see Figure 5c), the primary X line is located at $x\approx-19R_E$. On the earthward side of the primary X line, there exists a secondary X line at $x\approx-13.5R_E$. Between the two X lines, there forms an FR located around $x=-16R_E$. Because the reconnection rate at the primary X line is much faster, the positive B_z is much stronger than the negative B_z (Figure 5a). The secondary X line and the FR propagate earthward due to the driven of the high-speed earthward flow of the primary X line. When the earthward propagating FR moves across a satellite, the satellite will detect first negative (with smaller amplitude) then positive (with larger amplitude) B_z, as well as all the DF signatures shown in Figure 3. The typical ion number density in the magnetotail plasma sheet is about $0.05N_0$, so the local ion inertial length $d_i\approx0.45R_E$. The distance between the positive and negative B_z peaks is about $1.8R_E$; i.e., the DF thickness is about $4d_i$.

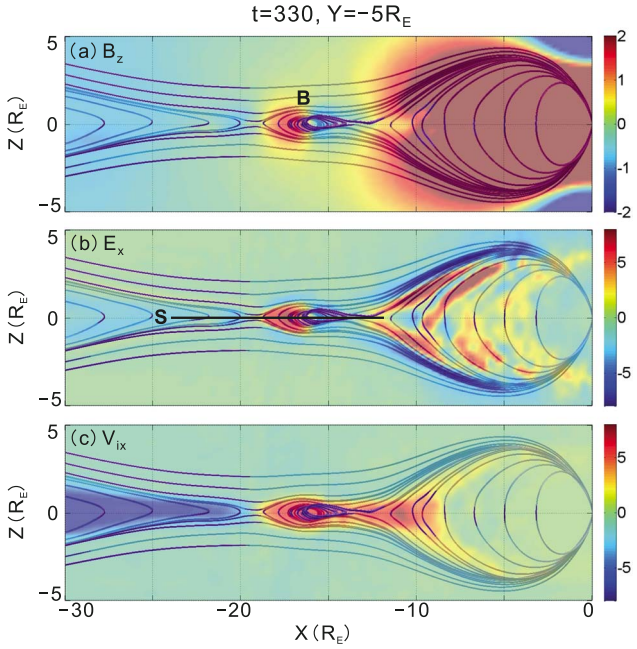

Figure 5. Magnetic field lines in 3-D perspective and contours of the (a) magnetic field B_z, (b) electric field E_x, and (c) ion flow velocity V_{ix} around DF-B in the (x,z) plane along $y=-5R_E$ at t=330.

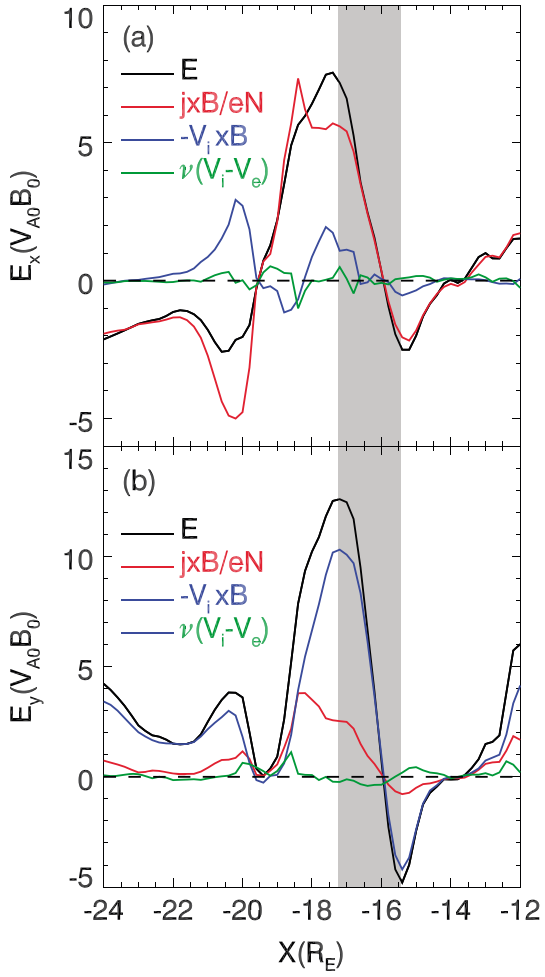

Figure 6. Spatial variations of (a) E_x and (b) E_y as well as the contributions of the Hall term $\mathbf{j}\times\mathbf{B}/Ne$, convection term $-\mathbf{V}_i\times\mathbf{B}$, and collision term $\nu(\mathbf{V}_i-\mathbf{V}_e)$ in the generalized Ohm's law along the line segment S marked in Figure 5b. The grey area signifies the region of DF-B.

Figure 6 shows the detailed structures of E_x (Figure 6a) and E_y (Figure 6b) as well as the contributions of the Hall term $\mathbf{j}\times\mathbf{B}/eN$, convection term $-\mathbf{V}_i\times\mathbf{B}$, and collision term $\nu(\mathbf{V}_i-\mathbf{V}_e)$ in the generalized Ohm's law [e.g., *Vasyliunas*, 1975] along the line segment S marked in Figure 5b. It shows that the normal electric field E_x is mainly contributed by the Hall term j_yB_z/eN, which is consistent with the THEMIS [*Zhou et al.*, 2009] and Cluster [*Fu et al.*, 2012a] observations. The current j_y is formed by the decoupling of electrons and ions (the electrons are mainly magnetized, and the ions are mainly unmagnetized) in the y direction. However, the electric field E_y around the DF is mainly contributed by the convection term $V_{ix}B_z$, and the Hall term $-j_xB_z/eN$ contributes little, which indicates that, in the x direction, the ions are still frozen-in and coupled with the electrons. The Hall effect (mainly in the y direction) dominates the physics around the DF. Note that the contribution of the collision/resistivity term (denoted by the green curves) to the electric field is very small. In general, magnetic reconnection is believed to be triggered by the electron kinetic effects [e.g., *Lu et al.*, 2013] which are not included in hybrid models. In our simulation, the small current-dependent collision frequency is imposed to model the electron kinetic anomalous resistivity and trigger magnetic reconnection. After the reconnection is triggered, the reconnection process is not sensitive to the resistivity used.

FRs/DFs are formed by multiple X line reconnection. As the FRs/DFs propagate earthward, reconnection at the secondary X line is gradually suppressed and evolves into antireconnection due to which the southward B_z of the FRs/DFs is eroded. Figure 7 shows the evolution of FR/DF-A. At $t=317$, FR/DF-A is situated at about $x=-15R_E$ and flanked by two X lines: the primary X line at $x\approx-18.5R_E$ and the secondary X line at $x\approx-13.5R_E$. Note that the reconnection at the two X lines is normal reconnection with the upstream plasma flow toward the reconnection sites. At $t=320$, the earthward propagating DF/FR-A has moved to about $x=-13R_E$, and the primary and secondary X lines have moved to $x\approx-17.5R_E$ and $x\approx-12R_E$, respectively. The reconnection at the primary X line is still normal reconnection. In contrast, at the secondary X line, the ion flow V_{iz} is away from the reconnection site, which indicates that the reconnection at the secondary X line has evolved into antireconnection. At the same time, the newly formed FR/DF-B is located at about $x=-18R_E$. At about $t=322$, DF/FR-A has almost merged into the near-Earth region through the antireconnection process.

More detailed B_z evolutions of FR/DF-A at $t=311$, 312, 316, 319, 321, and 322 are shown in Figure 8. At $t=311$ and $t=312$ when FR-A is newly formed, the magnetic field B_z is weak and less asymmetric. At $t=316$, B_z of FR-A has grown stronger and more asymmetric due to the imbalance of the reconnection rates between the primary and secondary X lines, with the maximum of about $1.2B_0$ and minimum of about $-0.35B_0$. At

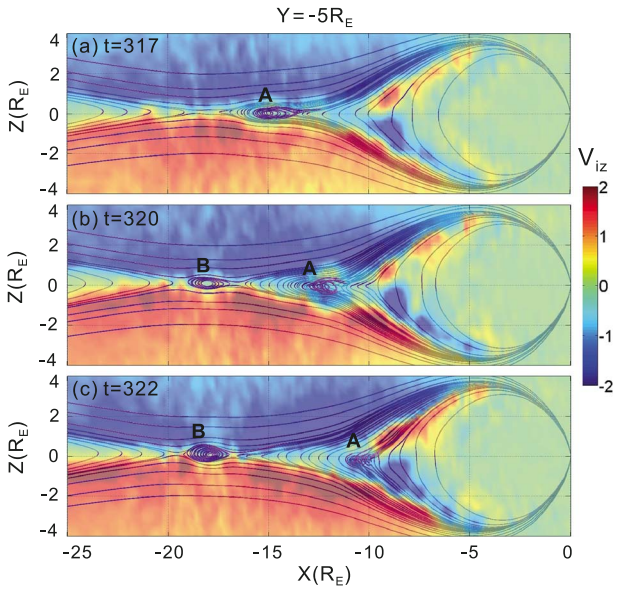

Figure 7. Magnetic field lines and contour of V_{iz} in the near-tail (x, z) plane along $y = -5R_E$ at t =(a) 317, (b) 320, and (c) 322.

t=319, the magnetic field B_z of FR-A is strongest. It should be noted that, at t=321, the negative B_z magnetic flux is less than that at t=319, and at t=322, the negative B_z magnetic flux vanished completely. The decrease and vanishment of the southward magnetic flux is due to the erosion caused by the antireconnection between the southward B_z and the northward geomagnetic field. As the magnetic field B_z of FR-A gradually becomes highly asymmetric, it evolves into a typical DF at the late stage of its evolution. Note that the slope of B_z at the front increases very fast from t=311 to t=312, and does not change much after t=312, which suggests that the sharp B_z front is formed at the very early stage by the multiple X line fast reconnection, not by the magnetic flux pileup process at the late stage. The imbalance of the reconnection rates between the primary and secondary X lines and the antireconnection at the later stage mainly cause the asymmetry of DF-A but do not cause the buildup of the sharp front.

Figure 9 presents the time evolutions of the northward (red) and southward (blue) magnetic fluxes of FR/DF-A at $y = -5R_E$, $z = 0$. The northward (southward) magnetic flux of FR/DF-A is generated by the reconnection at the primary (secondary) X line. At the early stage of the evolution of FR/DF-A (t=312), the northward magnetic flux is about $0.45B_0R_E$, and the southward is about $0.2B_0R_E$. The reconnection rate at the primary X line is much faster and keeps growing, which leads to the fast increase of the northward magnetic flux. In contrast, the reconnection at the secondary X line is suppressed, and the reconnection rate is much slower. At t=319, the southward magnetic flux reaches its maximum of about $0.7B_0R_E$, while the northward magnetic flux is much larger, about $2.3B_0R_E$. After t=319, the southward magnetic flux begins to decrease because of the erosion caused by the antireconnection at the secondary X line, while the northward magnetic flux keeps growing. By t=322, the southward magnetic flux has been fully eroded, and FR/DF-A has fully merged into the near-Earth region. Figure 10 shows the time evolutions of the location and earthward propagation speed of FR/DF-A. The FR/DF is formed at $x \approx -17R_E$ and eventually merges into the near-Earth region at $x \approx -11R_E$. The earthward propagation speed grows faster from about 150 km/s (at $x \approx -17R_E$ when t=312) to nearly 1000 km/s (at $x \approx -14R_E$ when t=319). The earthward acceleration of the DF is caused by the imbalance of the reconnection rates between the primary and secondary X lines.

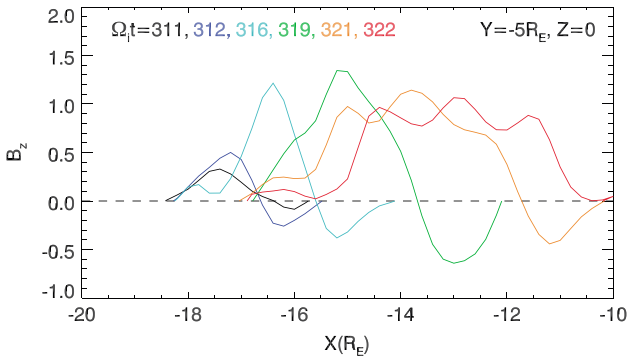

Figure 8. Structure of B_z around FR/DF-A along $y = -5R_E$, $z = 0$ at t =311, 312, 316, 319, 321, and 322.

Figure 11 demonstrates that the earthward propagating FRs/DFs can be highly tilted in the equatorial (z=0) plane with respect to the y axis during their evolution. At t=335, DF-B is tilted/kinked and shows a boomerang-like shape. The center of DF-B moves faster and is located at $(x, y) \approx (-12, -6)R_E$ (indicated by the green arrow), while the two flanks move slower and are located at $(x, y) \approx (-17, -3)R_E$ and $(-17, -10)R_E$

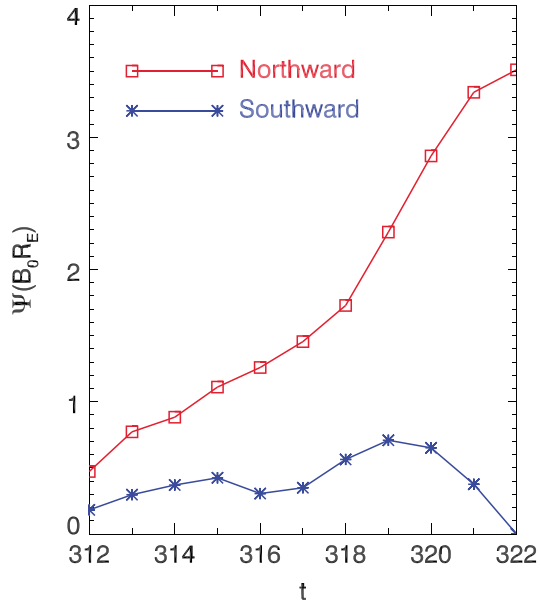

Figure 9. Time evolutions of the northward magnetic flux $\int_{B_z>0}|B_z|dx$ (red) and southward magnetic flux $\int_{B_z<0}|B_z|dx$ (blue) of FR/DF-A along $y=-5R_E$, $z=0$. Note that here we only consider a 2-D slice along $y=-5R_E$ for simplicity.

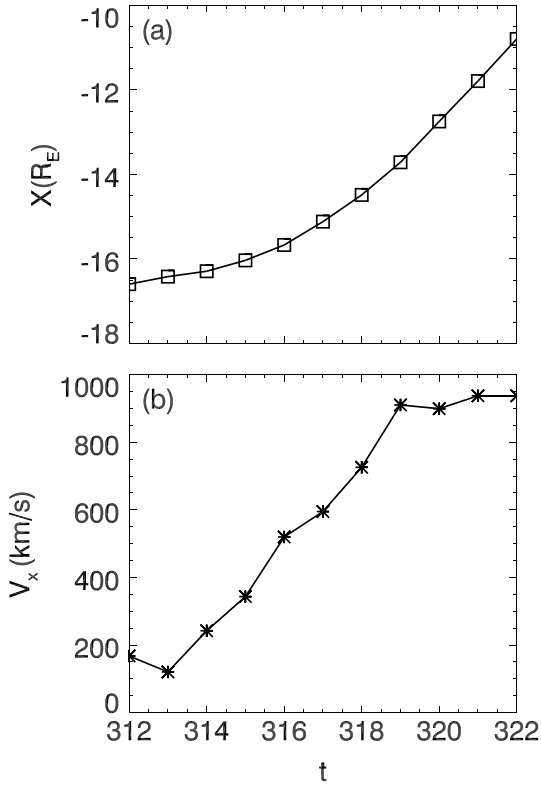

Figure 10. Time evolutions of the (a) location and (b) earthward propagation speed of DF-A. The location of the DF is where the northward magnetic field B_z begins to enhance sharply. Note that the scale length used in the simulation is 6.77 times larger than that in reality. Therefore, in the calculation of the propagation speed, the time is scaled back by a factor of 6.77 to fit in the real convection times.

(indicated by the yellow arrows), respectively. The primary reconnection X line is located at $x\approx-20R_E$ (see the series of the red dots around the equatorial plane). Our method of identification of X lines for the tail current sheet is the same as that described by *Tan et al.* [2011] and *Lin et al.* [2014] and consistent with the general procedure described by *Priest and Forbes* [2000]. When an X line that separates local areas of four different types of magnetic connectivity exists, the X type configuration of field lines can be located when mapping the 3-D field lines into an (x,z) reference plane. The point of the X line in the plane is marked by a red dot in Figure 11. An X line segment can be traced by connecting the X points in a series of such (x,z) planes. The evolution of the FR/DF is dominated by the reconnection rate at the primary X line which can be roughly given as $R\approx V_{in}/V_A$ (V_{in} is the inflow velocity). Not shown in this figure, near the primary X line, the inflow speed at $y=-6R_E$ is $V_{in}\approx 2V_{A0}$, while at $y=-3R_E$, the inflow speed $V_{in}\approx V_{A0}$. The ion density in the vicinity of the reconnection site is about $0.05N_0$, and the magnitude of the ambient magnetic field is about $3.5B_0$. Therefore, the local Alfvén speed near the reconnection site is $V_A\approx 15.65V_{A0}$, and thus, the reconnection rate at $y=-6R_E$ is $R\approx V_{in}/V_A\approx 0.13$, while at $y=-3R_E$, the reconnection rate is $R\approx V_{in}/V_A\approx 0.064$. The reconnection rate at the center is faster than that at the flank, which leads to the formation of a stronger BBF around $y=-6R_E$ and drives the center of FR/DF-B faster. The FR/DF tilt and nonuniformity in the dawn-dusk direction show the importance of the 3-D effects in the magnetotail.

4. Discussion

Recently, by applying magnetohydrostatic Grad-Shafranov reconstruction technique to an FR event and a DF event observed by THEMIS, *Vogiatzis et al.* [2015] suggest that there is a possibility that DFs are originated from highly dissipated FRs during the late stage of their

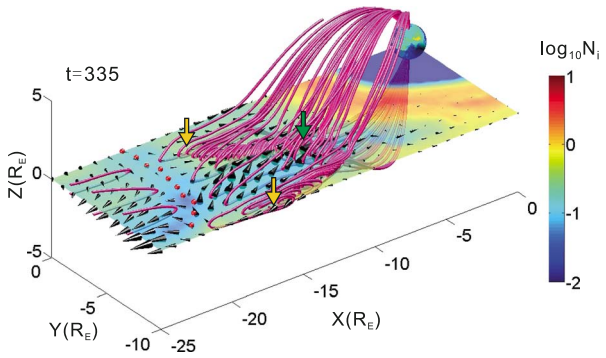

Figure 11. Magnetic field lines, ion flow vectors in 3-D perspective, and ion density $\log_{10}N_i$ contours in the zoomed near-tail reconnection and DF-B region at t =335. A series of red dots denotes the primary X line.

evolution. In the present study, we use a 3-D global hybrid simulation to show a similar scenario. The evolution process of the FR/DF is studied in detail, which can be described as follows. In the early stage, an FR is formed by multiple X line fast reconnection and shows a bipolar B_z structure. The reconnection rate difference between the primary and secondary X lines is small, so the asymmetry between the positive and negative B_z is weak at this stage. The sharp front of B_z is formed at the early stage by the fast reconnection in the center of the FR. In the later stage, the reconnection at the primary X line keeps growing, while the reconnection at the secondary X line is suppressed. Therefore, the imbalance of the reconnection rate between the primary and secondary X lines increases, which leads to the formation of a highly asymmetric B_z structure. When the FR approaches the near-Earth region, the reconnection at the secondary X line is fully suppressed and evolves into antireconnection between the preceding southward magnetic field of the DF and the northward geomagnetic field. The antireconnection leads to the erosion of the negative B_z, which further aggravates the B_z asymmetry. As the proceeding of the antireconnection, the DF eventually merges into the near-Earth dipole-like region. The imbalance of the reconnection rates between the primary and secondary X lines also leads to the earthward acceleration of the DF during its propagation.

On the formation of the DFs, there are three main mechanisms: (1) by transient magnetotail reconnection at ~ $20R_E$ [*Sitnov et al*., 2009; *Pritchett*, 2010; *Sitnov and Swisdak*, 2011; *Fu et al*., 2013]; (2) by jet braking in the near-Earth region ($r < 10R_E$, where r is the geocentric distance), in which the overshoot and rebounding of BBFs by the preexisting magnetic field and plasma in the near-Earth region leads to formation of vortices which associated to the formation of the DFs [*Birn et al*., 2011; *Nakamura et al*., 2013]; and (3) spontaneous formation due to some kinds of instability, such as kinetic ballooning/interchange instability [*Pritchett and Coroniti*, 2011] and ion-tearing mode instability [*Sitnov et al*., 2013]. In the present study, we show the scenario that the DFs are actually earthward propagating FRs; therefore, the DF/FR is formed by multiple X line fast reconnection. Around the center of the FR between the primary and secondary X lines, a sharp B_z front is formed by the compression of the reconnected magnetic flux. As shown in Figure 8, from t =311 to t =312, the magnetic field B_z is steepened very fast due to the multiple X line fast reconnection; after t =312, the slope of B_z is almost unchanged, which suggests that the further magnetic flux pileup in the later stage does not contribute to the DF formation. In summary, we propose that multiple X line reconnection is an alternative formation mechanism for DF as an earthward propagating FR. During its earthward propagation, the FR evolves into DF due to the imbalance of the reconnection rates between the primary and secondary X lines and the further dissipation of magnetic flux by antireconnection at the secondary X line. Nevertheless, the sharp front of B_z has already formed at the early stage by the multiple X line fast reconnection.

Based on our simulation, considering that the DFs are earthward propagating FRs, it is much easier to understand why there is a preceded negative B_z dip in front of the DFs: the negative B_z dip comes from the remaining southward magnetic field of the FRs that has not yet been fully eroded. Nevertheless, in spacecraft observations, the small B_z dip of the DFs is not always negative. A lot of DF events actually have a positive dip. *Schmid et al*. [2011] conduct a statistical study of DFs in the magnetotail and find that in the 107 DF events, 38 events have a negative B_z minimum value (dip). As shown in Figure 12a, an FR (FR-C) is situated in the core region of the DF. When the core region of the earthward propagating DF-C moves across a satellite (e.g., located at $(x, y, z) = (-12, 2, 0)R_E$), the satellite will detect a negative-then-positive B_z signature (the amplitude of the negative B_z is much smaller than the positive B_z), as shown in Figure 12b. On the other hand, if the outer region (upper or lower) without a helical flux rope moves across a satellite

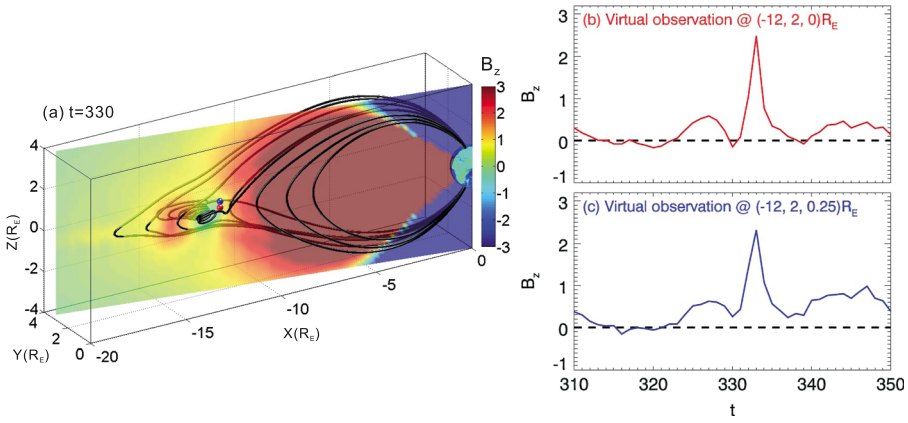

Figure 12. (a) Typical magnetic field lines of DF-C and contour of B_z in the $-10°$ meridian plane at t =330. The red and blue dots denote two virtual satellite located at $(x, y, z) = (-12, 2, 0)R_E$ and $(-12, 2, 0.25)R_E$. (b) Virtual satellite observation of the magnetic field B_z versus time at $(x, y, z) = (-12, 2, 0)R_E$. (c) Virtual satellite observation of the magnetic field B_z versus time at $(x, y, z) = (-12, 2, 0.25)R_E$.

(e.g., located at $(x, y, z) = (-12, 2, 0.25)R_E$), the satellite will also detect a sharp increase of B_z which is preceded by a smaller-amplitude B_z dip, but the dip is no longer negative (see Figure 12c). Hence, according to the above virtual satellite observations, both negative and positive B_z dips of the DF can be observed in our simulation, depending on the specific trajectory along which the satellite moves across the DF.

Sharp, highly asymmetric north-then-south bipolar variations (with larger southward portion) in the magnetic B_z component have recently been observed by ARTEMIS in the midtail region by *Li et al.* [2014]. These tailward moving sharp fronts are very similar to those of classical, typically earthward moving DFs, except for their B_z polarity and flow direction. Therefore, they are called "antidipolarization fronts" (ADFs). The ADFs are found to be related to plasmoids/FRs during their tailward propagation. In our simulation, the tailward FRs are also formed in the near-tail region through multiple X line reconnection. Figure 13a shows a typical tailward propagating FR which is located around $(x, y, z) = (-21, -1, 0)R_E$. Similar to the earthward propagating FRs, the tailward propagating FR is also flanked by two X lines, the primary X line (with a higher reconnection rate) at $x \approx -18R_E$ and the secondary X line (with a lower reconnection rate) at $x \approx -23.5R_E$. The FR and secondary X line move tailward due to the tailward high-speed outflow of the primary X line. The magnetic field B_z is also asymmetric because of the imbalance of the reconnection rates between the primary and secondary X lines, with the southward/negative B_z stronger than the northward/positive B_z. Assuming that there is a satellite located in the path of the tailward propagating FR (e.g., located at $(x, y, z) = (-21, -1, 0)R_E$), it will detect a positive-then-negative bipolar variation (with a larger negative portion) as shown in Figure 13b, namely, the ADF. Figure 13b shows the virtual satellite observations at $(x, y, z) = (-21, -1, 0)R_E$. The flow enhancement is now mainly in the tailward direction, and the normal electric field component E_x is now negative. Here we suggest that the ADFs are likely to be tailward propagating FRs, analogous to the DFs as earthward propagating FRs. In observations, both the earthward and tailward propagating FRs are frequently observed in the magnetotail [*Slavin et al.*, 2003; *Imber et al.*, 2011]. Some of them may evolve into the earthward propagating DFs and tailward propagating ADFs.

Based on the spacecraft observations, the thickness of the DFs is on the order of ion kinetic scales [*Sergeev et al.*, 2009; *Schmid et al.*, 2011; *Fu et al.*, 2012a]; therefore, the ions are demagnetized while the electrons are magnetized and frozen in the magnetic field lines. The motions of ions and electrons are decoupled, which leads to the generation of the Hall effects [*Zhou et al.*, 2009; *Fu et al.*, 2012a]. Recently, 3-D global-scale MHD simulations have also been performed to investigate the DFs in the magnetotail [*Ge et al.*, 2011, 2012; *Ashour-Abdalla et al.*, 2011; *Pan et al.*, 2014a, 2014b]. However, in these MHD simulations, the reconnection in the magnetotail is not sufficiently fast to drive a DF directly, and the thin (ion kinetic scale) DF cannot be resolved. Compared with the 3-D global MHD models, our 3-D global hybrid simulation model can fully resolve the Hall physics and fast reconnection, which generates the thin DFs (on the order of several ion inertial lengths).

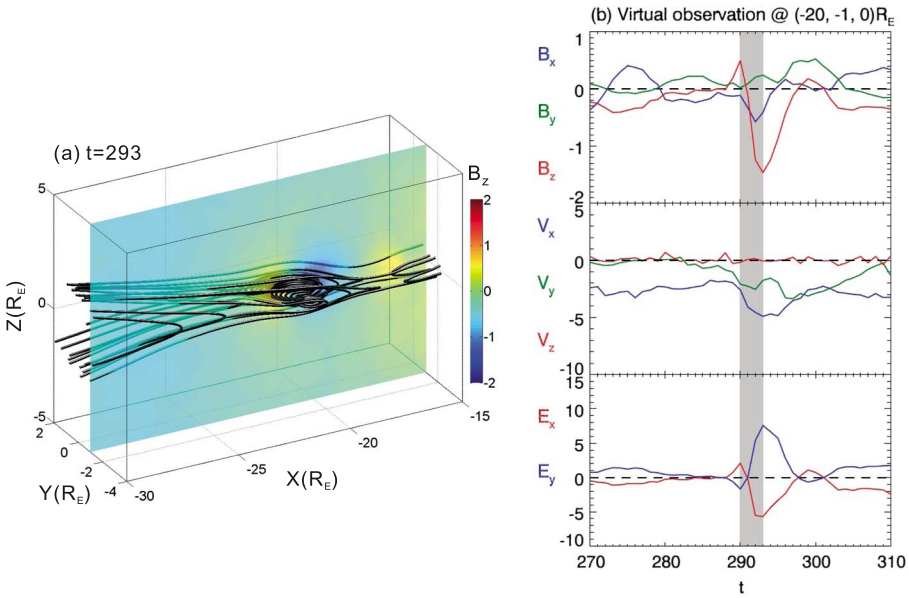

Figure 13. (a) Typical magnetic field lines of an antidipolarization front (ADF) and contours of B_z in the (x, z) plane along $y = -1\ R_E$ at t =293. (b) Virtual satellite observations of the magnetic field components B_x, B_y, and B_z; ion flow velocities V_{ix}, V_{iy}, and V_{iz}; and electric field components E_x and E_y versus time at $(x, y, z) = (-21, -1, 0)R_E$. The grey area signifies the region of ADF.

In spacecraft observations, the earthward propagation speed of DFs is estimated to be 300 km/s [*Runov et al*., 2009, 2011b]. Moreover, previous two-dimensional (2-D) local-scale particle-in-cell simulations also show that the DFs propagate away from the X line with an approximately constant speed [*Sitnov et al*., 2009; *Wu and Shay*, 2012]. In contrast, in our global hybrid simulation, we have demonstrated that the propagation speed increases during the earthward propagation of the DFs. In the near tail where the DFs are newly formed, the propagation speed is lower (about 150 km/s); when the DFs move close to the near-Earth region, the propagation speed is much faster (nearly 1000 km/s). Moreover, we have further demonstrated that the DFs (or earthward propagating FRs) eventually merge into the near-Earth region through antireconnection. Through the merging process of the DFs (or earthward propagating FRs) in the near-Earth region, magnetic flux and plasmas are injected into and piled up in front of the inner magnetosphere, which leads to the global-scale dipolarization [*Hesse and Birn*, 1991; *Baumjohann et al*., 1999; *Lin et al*., 2014]. The merging of the fast earthward propagating DFs/FRs can also lead to the generation of the kinetic compressional waves in the near-Earth region [*Lin et al*., 2014]. It is also found in our simulation that the ions are strongly energized by the DFs.

Large IMF B_y can be penetrated into the magnetotail plasma sheet and therefore results in a large guide field for reconnection [e.g., *Petrukovich*, 2011; *Rong et al*., 2012; *Teh et al*., 2014]. In contrast, in our simulation, the IMF B_y is zero, which leads to the scenario of nearly zero guide field magnetotail reconnection. In the nearly zero guide field reconnection, the core field B_y of the generated FRs is also very small, and the magnitude of the magnetic field has a crater-like structure near the center of the FRs [*Lu et al*., 2015]. Several possible mechanisms have been suggested for the generation of the core field. One is that the core field of the FRs originates from a compression of the preexisting seed guide field of reconnection [*Karimabadi et al*., 1999; *Drake et al*., 2006; *Markidis et al*., 2013]. Another mechanism that relies on the collapse or pinching of the FRs to achieve a large core field is proposed by *Hesse et al*. [1996]. In our simulation, the guide field of the magnetotail reconnection is nearly zero, and the core field of the FRs is also weak. The simulation result may be favorable to the first mechanism. The correlation of the core field and the IMF B_y has also been studied by spacecraft observations [e.g., *Slavin et al*., 2003; *Borg et al*., 2012; *Teh et al*., 2014]. In spite of the theoretical and observational efforts, the generation mechanism of the core field in FRs is still unclear and needs further investigations.

5. Summary

In this paper, a 3-D global hybrid simulation model is utilized to study the formation, structure, and evolution of the DFs as earthward propagating FRs in the magnetotail. It is found that small-scale FRs are formed by multiple X line reconnection in the near tail ($x \approx -20R_E$), and they then propagate earthward to the near-Earth region ($r < 10R_E$). Based on the virtual satellite observations, the earthward propagating FRs in our simulation can fully reproduce the observational features of the DFs, e.g., a sharp enhancement of B_z, a smaller amplitude preceding B_z dip, an earthward flow enhancement, electric field components in the normal and dawn-dusk directions, and the ion energization. Therefore, we suggest that the earthward FRs can be used to explain the DFs, at least some of the DFs, observed in the magnetotail. The thickness of the DFs is about $4d_i$ (d_i is the local ion inertial length in the magnetotail plasma sheet), and the electric field directed normal to the front is found to be dominated by the Hall physics. The DFs can be tilted in the GSM (x, y) plane with respect to the y axis and only extend several Earth radii in the y direction. The formation, structure, and evolution of the DFs are nonuniform in the dawn-dusk direction, which indicates that the DFs are essentially 3-D. During the earthward propagation from the near-tail ($x \approx -20R_E$) to the near-Earth region ($x \approx -10R_E$), the speed of the DFs grows faster from ~150 km/s to ~1000 km/s. Eventually, the DFs merge into the near-Earth dipole-like region through antireconnection between the preceding southward/negative B_z of the DFs and the northward/positive geomagnetic field.

Acknowledgments

This work was supported by 973 Program (2012CB825602 and 2013CBA01503); the National Science Foundation of China grants 41474125, 41331067, 11235009, 41274124, 41274144, and 41121003; CAS Key Research Program KZZD-EW-01-4; and NSF grant AGS 1405225 to Auburn University. Computer resources were provided by the National Supercomputer Center of China in Tianjin and Alabama Supercomputer Center. The results in this paper are generated from our computer simulation code as described in section 2. The data can be obtained by contacting the corresponding author through e-mail.

Michael Liemohn thanks Ioannis Vogiatzis and another reviewer for their assistance in evaluating this paper.

References

Angelopoulos, V., C. F. Kennel, F. V. Coroniti, R. Pellat, M. G. Kivelson, R. J. Walker, C. T. Russell, W. Baumjohann, W. C. Feldman, and J. T. Gosling (1994), Statistical characteristics of bursty bulk flow events, *J. Geophys. Res.*, *99*, 21,257–21,280, doi:10.1029/94JA01263.

Artemyev, A. V., V. N. Lutsenko, and A. A. Petrukovich (2012), Ion resonance acceleration by dipolarization fronts: Analytic theory and spacecraft observation, *Ann. Geophys.*, *30*, 317–324, doi:10.5194/angeo-30-317-2012.

Ashour-Abdalla, M., M. El-Alaoui, M. L. Goldstein, M. Zhou, D. Schriver, R. Richard, R. Walker, M. G. Kivelson, and K. Hwang (2011), Observations and simulations of non-local acceleration of electrons in magnetotail magnetic reconnection events, *Nat. Phys.*, *7*, 360–365, doi:10.1038/nphys1903.

Baker, D. N., T. I. Pulkkinen, V. Angelopoulos, W. Baumjohann, and R. L. McPherron (1996), Neutral line model of substorms: Past results and present view, *J. Geophys. Res.*, *101*, 12,975–13,010, doi:10.1029/95JA03753.

Baumjohann, W., M. Hesse, S. Kokubun, T. Mukai, T. Nagai, and A. A. Petrukovich (1999), Substorm dipolarization and recovery, *J. Geophys. Res.*, *104*, 24,995–25,000, doi:10.1029/1999JA900282.

Birn, J., R. Nakamura, E. V. Panov, and M. Hesse (2011), Bursty bulk flows and dipolarization in MHD simulations of magnetotail reconnection, *J. Geophys. Res.*, *116*, A01210, doi:10.1029/2010JA016083.

Birn, J., A. Runov, and M. Hesse (2014), Energetic electrons in dipolarization events: Spatial properties and anisotropy, *J. Geophys. Res. Space Physics*, *119*, 3604–3616, doi:10.1002/2013JA019738.

Borg, A. L., M. G. G. Taylor, and J. P. Eastwood (2012), Observations of magnetic flux ropes during magnetic reconnection in the Earth's magnetotail, *Ann. Geophys.*, *30*, 761–773, doi:10.5149/angeo-30-761-2012.

Daughton, W., V. Roytershteyn, H. Karimabadi, L. Yin, B. J. Albright, B. Bergen, and K. J. Bowers (2011), Role of electron physics in the development of turbulent magnetic reconnection in collisionless plasmas, *Nat. Phys.*, *7*, 539–542, doi:10.1038/NPHYS1965.

Deng, X. H., M. Ashour-Abdalla, M. Zhou, R. Walker, M. El-Alaoui, V. Angelopoulos, R. E. Ergun, and D. Schriver (2010), Wave and particle characteristics of earthward electron injections associated with dipolarization fronts, *J. Geophys. Res.*, *115*, A09225, doi:10.1029/2009JA015107.

Drake, J. F., M. S. Swisdak, K. M. Schoeffler, B. N. Rogers, and S. Kobayashi (2006), Formation of secondary islands during magnetic reconnection, *Geophys. Res. Lett.*, *33*, L13105, doi:10.1029/2006GL025957.

Eastwood, J. P., D. G. Sibeck, J. A. Slavin, M. L. Goldstein, B. Lavraud, M. Sitnov, S. Imber, A. Balogh, E. A. Lucek, and I. Dandouras (2005), Observations of multiple X-line structure in the Earth's magnetotail current sheet: A Cluster case study, *Geophys. Res. Lett.*, *32*, L11105, doi:10.1029/2005GL022509.

Fu, H. S., Y. V. Khotyaintsev, M. André, and A. Vaivads (2011), Fermi and betatron acceleration of suprathermal electrons behind dipolarization fronts, *Geophys. Res. Lett.*, *38*, L16104, doi:10.1029/2011GL048528.

Fu, H. S., Y. V. Khotyaintsev, A. Vaivads, M. André, and S. Y. Huang (2012a), Electric structure of dipolarization front at sub-proton scale, *Geophys. Res. Lett.*, *39*, L06105, doi:10.1029/2012GL051274.

Fu, H. S., Y. V. Khotyaintsev, A. Vaivads, M. André, and S. Y. Huang (2012b), Occurrence rate of earthward-propagating dipolarization fronts, *Geophys. Res. Lett.*, *39*, L10101, doi:10.1029/2012GL051784.

Fu, H. S., et al. (2013), Dipolarization fronts as a consequence of transient reconnection: In situ evidence, *Geophys. Res. Lett.*, *40*, 6023–6027, doi:10.1002/2013GL058620.

Ge, Y. S., J. Raeder, V. Angelopoulos, M. L. Gilson, and A. Runov (2011), Interaction of dipolarization fronts within multiple bursty bulk flows in global MHD simulations of a substorm on 27 February 2009, *J. Geophys. Res.*, *116*, A00I23, doi:10.1029/2010JA015758.

Ge, Y. S., X. Z. Zhou, J. Liang, J. Raeder, M. L. Gilson, E. F. Donovan, V. Angelopoulos, and A. Runov (2012), Dipolarization fronts and associated auroral activities: 1. Conjugated observations and perspectives from global MHD simulation, *J. Geophys. Res.*, *117*, A10226, doi:10.1029/2012JA017676.

Hamrin, M., et al. (2013), The evolution of flux pileup regions in the plasma sheet: Cluster observations, *J. Geophys. Res. Space Physics*, *118*, 6279–6290, doi:10.1002/jgra.50603.

Hesse, M., and J. Birn (1991), On dipolarization and its relation to the substorm current wedge, *J. Geophys. Res.*, *96*, 19,417–19,426, doi:10.1029/91JA01953.

Hesse, M., J. Birn, M. M. Kuznetsova, and J. Dreher (1996), A simple model of core field generation during plasmoid evolution, *J. Geophys. Res.*, *101*, 10,797–10,804, doi:10.1029/95JA03149.

Hones, E. W. (1977), Substorm processes in magnetotail: Comments on "On hot tenuous plasmas, fireballs, and boundary-layers in Earth's magnetotail" by L. A. Frank et al, *J. Geophys. Res.*, *82*, 5633–5640, doi:10.1029/JA082i035p05633.

Imber, S. M., J. A. Slavin, H. U. Auster, and V. Angelopoulos (2011), A THEMIS survey of flux ropes and traveling compression regions: Location of the near-Earth reconnection site during solar minimum, *J. Geophys. Res.*, *116*, A02201, doi:10.1029/2010JA016026.

Karimabadi, H., D. Krauss-Varban, N. Omidi, and H. X. Vu (1999), Magnetic structure of the reconnection layer and core field generation in plasmoids, *J. Geophys. Res.*, *104*, 12,313–12,326, doi:10.1029/1999JA900089.

Kuznetsova, M. M., M. Hesse, and D. Winske (2001), Collisionless reconnection supported by nongyrotropic pressure effects in hybrid and particle simulations, *J. Geophys. Res.*, *106*, 3799–3810, doi:10.1029/1999JA001003.

Lee, L. C., and Z. F. Fu (1985), A theory of magnetic-flux transfer at the Earth's magnetopause, *Geophys. Res. Lett.*, *12*, 105–108, doi:10.1029/GL012i002p00105.

Li, S. S., J. Liu, V. Angelopoulos, A. Runov, X. Z. Zhou, and S. A. Kiehas (2014), Antidipolarization fronts observed by ARTEMIS, *J. Geophys. Res. Space Physics*, *119*, 7181–7198, doi:10.1002/2014JA020062.

Lin, Y., X. Y. Wang, S. Lu, J. D. Perez, and Q. M. Lu (2014), Investigation of storm-time magnetotail and ion injection using three-dimensional global hybrid simulation, *J. Geophys. Res. Space Physics*, *119*, 7413–7432, doi:10.1002/2014JA020005.

Lu, Q. M., S. Lu, C. Huang, M. Y. Wu, and S. Wang (2013), Self-reinforcing process of the reconnection electric field in the electron diffusion region and onset of collisionless magnetic reconnection, *Plasma Phys. Control. Fusion*, *55*, 085019, doi:10.1088/0741-3333/55/8/085019.

Lu, S., Y. Lin, Q. M. Lu, X. Y. Wang, R. S. Wang, C. Huang, M. Y. Wu, and S. Wang (2015), Evolution of flux ropes in the magnetotail: A three-dimensional global hybrid simulation, *Phys. Plasmas*, *22*, 052901, doi:10.1063/1.4919615.

Markidis, S., P. Henri, G. Lapenta, A. Divin, M. Goldman, D. Newman, and E. Laure (2013), Kinetic simulations of plasmoid chain dynamics, *Phys. Plasma*, *20*, 082105, doi:10.1063/1.4817286.

Moldwin, M. B., and W. J. Hughes (1991), Plasmoids as magnetic-flux ropes, *J. Geophys. Res.*, *96*, 14,051–14,064, doi:10.1029/91JA01167.

Moldwin, M. B., and W. J. Hughes (1994), Observations of earthward and tailward propagating flux rope plasmoids: Expanding the plasmoid model of geomagnetic substorms, *J. Geophys. Res.*, *99*, 183–198, doi:10.1029/93JA02102.

Nakamura, R., et al. (2002), Motion of the dipolarization front during a flow burst event observed by Cluster, *Geophys. Res. Lett.*, *29*(20), 1942, doi:10.1029/2002GL015763.

Nakamura, R., et al. (2011), Flux transport, dipolarization, and current sheet evolution during a double-onset substorm, *J. Geophys. Res.*, *116*, A00I36, doi:10.1029/2010JA015865.

Nakamura, R., et al. (2013), Flow bouncing and electron injection observed by Cluster, *J. Geophys. Res. Space Physics*, *118*, 2055–2072, doi:10.1002/jgra.50134.

Ohtani, S. I., M. A. Shay, and T. Mukai (2004), Temporal structure of the fast convective flow in the plasma sheet: Comparison between observations and two-fluid simulations, *J. Geophys. Res.*, *109*, A03210, doi:10.1029/2003JA010002.

Oka, M., T. D. Phan, S. Krucker, M. Fujimoto, and I. Shinohara (2010), Electron acceleration by multi-island coalescence, *Astrophys. J.*, *714*, 915–926, doi:10.1088/0004-637X/714/1/915.

Omidi, N., X. Blanco-Cano, C. T. Russell, and H. Karimabadi (2006), Dipolar magnetospheres and their characterization as a function of magnetic moment, *Adv. Space Res.*, *33*, 1996–2003.

Pan, Q. J., M. Ashour-Abdalla, R. J. Walker, and M. El-Alaoui (2014a), Electron energization and transport in the magnetotail during substorms, *J. Geophys. Res. Space Physics*, *119*, 1060–1079, doi:10.1002/2013JA019508.

Pan, Q. J., M. Ashour-Abdalla, R. J. Walker, and M. El-Alaoui (2014b), Ion energization and transport associated with magnetic dipolarizations, *Geophys. Res. Lett.*, *41*, 5717–5726, doi:10.1002/2014GL061209.

Petrukovich, A. A. (2011), Origins of plasma sheet B_y, *J. Geophys. Res.*, *116*, A07217, doi:10.1029/2010JA016386.

Priest, E. R., and T. Forbes (2000), Definition of reconnection, in *Magnetic Reconnection: MHD Theory and Applications*, pp. 231–245, Cambridge Univ. Press, Cambridge, U. K.

Pritchett, P. L. (2010), Onset of magnetic reconnection in the presence of a normal magnetic field: Realistic ion to electron mass ratio, *J. Geophys. Res.*, *115*, A06301, doi:10.1029/2009JA01475.

Pritchett, P. L., and F. V. Coroniti (2011), Plasma sheet disruption by interchange-generated flow intrusions, *Geophys. Res. Lett.*, *38*, L10102, doi:10.1029/2011GL047527.

Rong, Z. J., et al. (2012), Profile of strong magnetic field B_y component in magnetotail current sheets, *J. Geophys. Res.*, *117*, A06216, doi:10.1029/2011JA017402.

Runov, A., V. Angelopoulos, M. I. Sitnov, V. A. Sergeev, J. Bonnell, J. P. McFadden, D. Larson, K. H. Glassmeier, and U. Auster (2009), THEMIS observations of an earthward-propagating dipolarization front, *Geophys. Res. Lett.*, *36*, L14106, doi:10.1029/2009GL038980.

Runov, A., V. Angelopoulos, X. Z. Zhou, X. J. Zhang, S. Li, F. Plaschke, and J. Bonnell (2011a), A THEMIS multicase study of dipolarization fronts in the magnetotail plasma sheet, *J. Geophys. Res.*, *116*, A05216, doi:10.1029/2010JA016316.

Runov, A., et al. (2011b), Dipolarization fronts in the magnetotail plasma sheet, *Planet. Space Sci.*, *59*, 517–525, doi:10.1016/j.pss.2010.06.006.

Schindler, K. (1974), A theory of the substorm mechanism, *J. Geophys. Res.*, *79*, 2803–2810, doi:10.1029/JA079i019p02803.

Schmid, D., M. Volwerk, R. Nakamura, W. Baumjohann, and M. Heyn (2011), A statistical and event study of magnetotail dipolarization fronts, *Ann. Geophys.*, *29*, 1537–1547, doi:10.5194/angeo-29-1537-2011.

Sergeev, V., V. Angelopoulos, S. Apatenkov, J. Bonnell, R. Ergun, R. Nakamura, J. McFadden, D. Larson, and A. Runov (2009), Kinetic structure of the sharp injection/dipolarization front in the flow-braking region, *Geophys. Res. Lett.*, *36*, L21105, doi:10.1029/2009GL040658.

Sitnov, M. I., and M. Swisdak (2011), Onset of collisionless magnetic reconnection in two-dimensional current sheets and formation of dipolarization fronts, *J. Geophys. Res.*, *116*, A12216, doi:10.1029/2011JA016920.

Sitnov, M. I., M. Swisdak, and A. V. Divin (2009), Dipolarization fronts as a signature of transient reconnection in the magnetotail, *J. Geophys. Res.*, *114*, A04202, doi:10.1029/2008JA013980.

Sitnov, M. I., N. Buzulukova, M. Swisdak, V. G. Merkin, and T. E. Moore (2013), Spontaneous formation of dipolarization fronts and reconnection onset in the magnetotail, *Geophys. Res. Lett.*, *40*, 22–27, doi:10.1029/2012GL054701.

Slavin, J. A., R. P. Lepping, J. Gjerloev, D. H. Fairfield, M. Hesse, C. J. Owen, M. B. Moldwin, T. Nagai, A. Ieda, and T. Mukai (2003), Geotail observations of magnetic flux ropes in the plasma sheet, *J. Geophys. Res.*, *108*(A1), 1015, doi:10.1029/2002JA009557.

Tan, B., Y. Lin, J. D. Perez, and X. Y. Wang (2011), Global-scale hybrid simulation of dayside magnetic reconnection under southward IMF: Structure and evolution of reconnection, *J. Geophys. Res.*, *116*, A02206, doi:10.1029/2010JA015580.

Teh, W. L., R. Nakamura, H. Karimabadi, W. Baumjohann, and T. L. Zhang (2014), Correlation of core field polarity of magnetotail flux ropes with the IMF B_y: Reconnection guide field dependency, *J. Geophys. Res. Space Physics*, *119*, 2933–2944, doi:10.1002/2013JA019454.

Vasyliunas, V. M. (1975), Theoretical models of magnetic field line merging, 1, *Rev. Geophys.*, *13*, 303–336, doi:10.1029/RG013i001p00303.

Vogiatzis, I. I., O. E. Malandraki, Q. G. Zong, X. Z. Zhou, T. E. Sarris, E. T. Sarris, H. Zhang, and T. A. Fritz (2011), THEMIS observations of earthward convected flux ropes triggering field dipolarization/substorm expansion and associated particle energization, *Ann. Geophys.*, *29*, 2117–2130, doi:10.5194/angeo-29-2117-2011.

Vogiatzis, I. I., A. Isavnin, Q. G. Zong, E. T. Sarris, S. W. Lu, and A. M. Tian (2015), Dipolarization fronts in the near-Earth space and substorm dynamics, *Ann. Geophys.*, *33*, 63–74, doi:10.5194/angeo-33-63-2015.

Volwerk, M., et al. (2008), Magnetotail dipolarization and associated current systems observed by Cluster and Double Star, *J. Geophys. Res.*, *113*, A08S90, doi:10.1029/2007JA012729.

Wang, R. S., Q. M. Lu, A. M. Du, and S. Wang (2010a), In situ observations of a secondary magnetic island in an ion diffusion region and associated energetic electrons, *Phys. Rev. Lett.*, *104*(17), 175003, doi:10.1103/Physrevlett.104.175003.

Wang, R. S., Q. M. Lu, X. Li, C. Huang, and S. Wang (2010b), Observations of energetic electrons up to 200 keV associated with a secondary island near the center of an ion diffusion region: A Cluster case study, *J. Geophys. Res.*, *115*, A11201, doi:10.1029/2010JA015473.

Wu, M. Y., Q. M. Lu, M. Volwerk, Z. Vörös, T. L. Zhang, L. C. Shan, and C. Huang (2013), A statistical study of electron acceleration behind the dipolarization fronts in the magnetotail, *J. Geophys. Res. Space Physics*, *118*, 4804–4810, doi:10.1002/jgra.50456.

Wu, P., and M. A. Shay (2012), Magnetic dipolarization front and associated ion reflection: Particle-in-cell simulations, *Geophys. Res. Lett.*, *39*, L08107, doi:10.1029/2012GL051486.

Zhou, M., M. Ashour-Abdalla, X. Deng, D. Schriver, M. El-Alaoui, and Y. Pang (2009), THEMIS observation of multiple dipolarization fronts and associated wave characteristics in the near-Earth magnetotail, *Geophys. Res. Lett.*, *36*, L20107, doi:10.1029/2009GL040663.

Zhou, X. Z., V. Angelopoulos, V. A. Sergeev, and A. Runov (2010), Accelerated ions ahead of earthward propagating dipolarization fronts, *J. Geophys. Res.*, *115*, A00I03, doi:10.1029/2010JA015481.

Zhu, Z. W., and R. M. Winglee (1996), Tearing instability, flux ropes, and the kinetic current sheet kink instability in the Earth's magnetotail: A three-dimensional perspective from particle simulations, *J. Geophys. Res.*, *101*, 4885–4897, doi:10.1029/95JA03144.

Zong, Q. G., et al. (2004), Cluster observations of earthward flowing plasmoid in the tail, *Geophys. Res. Lett.*, *31*, L18803, doi:10.1029/2004GL020692.